Applied Physics Letters

Room temperature terahertz quantum cascade laser source based on intracavity difference-frequency generation

Cite as: Appl. Phys. Lett. **92**, 201101 (2008); https://doi.org/10.1063/1.2919051
Submitted: 08 March 2008 . Accepted: 04 April 2008 . Published Online: 19 May 2008

Mikhail A. Belkin, Federico Capasso, Feng Xie, Alexey Belyanin, Milan Fischer, Andreas Wittmann, and Jérôme Faist

View Online

Export Citation

ARTICLES YOU MAY BE INTERESTED IN

Room temperature single-mode terahertz sources based on intracavity difference-frequency generation in quantum cascade lasers
Applied Physics Letters **99**, 131106 (2011); https://doi.org/10.1063/1.3645016

Terahertz sources based on Čerenkov difference-frequency generation in quantum cascade lasers
Applied Physics Letters **100**, 251104 (2012); https://doi.org/10.1063/1.4729042

Room temperature quantum cascade lasers with 27% wall plug efficiency
Applied Physics Letters **98**, 181102 (2011); https://doi.org/10.1063/1.3586773

Lock-in Amplifiers up to 600 MHz

AIP Publishing

© 2008 American Institute of Physics.

APPLIED PHYSICS LETTERS **92**, 201101 (2008)

Room temperature terahertz quantum cascade laser source based on intracavity difference-frequency generation

Mikhail A. Belkin,[1,a)] Federico Capasso,[1,b)] Feng Xie,[2] Alexey Belyanin,[2] Milan Fischer,[3] Andreas Wittmann,[3] and Jérôme Faist[3]
[1]*Harvard School of Engineering and Applied Sciences, Harvard University, Cambridge, Massachusetts 02138, USA*
[2]*Department of Physics, Texas A&M University, College Station, Texas 77843, USA*
[3]*Institute of Quantum Electronics, ETH Zürich, CH-8093 Zürich, Switzerland*

(Received 8 March 2008; accepted 4 April 2008; published online 19 May 2008)

We report on our progress in the development of a terahertz quantum cascade laser source based on intracavity terahertz difference-frequency mixing in a dual-wavelength mid-infrared quantum cascade laser with the active region engineered to possess giant second-order nonlinear susceptibility. In this letter, we demonstrate devices that operate in mid-infrared at $\lambda_1 = 8.9\ \mu$m and $\lambda_2 = 10.5\ \mu$m and produce terahertz output at $\lambda \approx 60\ \mu$m via difference-frequency generation with 7 μW output power at 80 K, 1 μW output at 250 K, and still approximately 300 nW output at 300 K. © *2008 American Institute of Physics*. [DOI: 10.1063/1.2919051]

The terahertz (THz) spectral range ($\lambda = 30-300\ \mu$m) has long been devoid of electrically pumped room temperature (RT) semiconductor source.[1–4] Despite recent progress with THz quantum cascade lasers (QCLs), existing devices still require cryogenic cooling.[2–4] An alternative way to produce THz radiation at RT is difference-frequency generation (DFG) in a nonlinear optical crystal using infrared (IR) or visible pump lasers.[5,6] Recently, we reported THz QCL sources based on intracavity DFG in dual-wavelength mid-IR QCLs with giant optical nonlinearity monolithically integrated in the active region.[7] Since mid-IR QCLs have been shown to operate continuous wave (cw) with more than 1.5 W of output power at RT (Ref. 8) and the optical nonlinearity for DFG is not expected to significantly deteriorate with temperature, this approach can lead to an electrically pumped cw RT semiconductor THz source.

DFG is a nonlinear optical process in which two beams at frequencies ω_1 and ω_2 interact in a medium with effective second-order nonlinear susceptibility $\chi^{(2)}$ to produce radiation at frequency $\omega_3 = \omega_1 - \omega_2$. The power of the latter is given by the expression[5,7,9]

$$W(\omega_3 = \omega_1 - \omega_2) = \frac{\omega_3^2}{8\varepsilon_0 c^3 n(\omega_1)n(\omega_2)n(\omega_3)} |\chi^{(2)}|^2 \frac{W(\omega_1)W(\omega_2)}{S_{\text{eff}}} l_{\text{coh}}^2, \quad (1)$$

where $l_{\text{coh}} = 1/[|\vec{k}_3 - (\vec{k}_1 - \vec{k}_2)|^2 + (\alpha/2)^2]$ is the coherence length, $W(\omega_i)$, $n(\omega_i)$, and $\vec{k}_i$ are the power, refractive index, and the wave vector of the beam at frequency ω_i, respectively, α stands for the losses at DFG frequency, and S_{eff} is the effective area of interaction. Following Eq. (1), for efficient DFG, one needs to use materials with large $\chi^{(2)}$, input beams of high intensity, and achieve low losses and phase matching, $|\vec{k}_3 - (\vec{k}_1 - \vec{k}_2)| \approx 0$. For intracavity DFG in an electrically pumped semiconductor laser, the intensities of the pump beams are limited to ~ 10 MW/cm^2 and l_{coh} is limited to hundreds of microns by free carrier absorption at THz frequency. Under these circumstances, it is only possible to achieve efficient THz DFG if $\chi^{(2)}$ in the laser is orders of magnitude larger than that in typical nonlinear crystals.[7]

Large $\chi^{(2)}$ in quantum well structures can be achieved by tailoring them so that all interacting fields are in resonance with intersubband transitions.[10] This approach typically results in a strong absorption of the pump beams, unless the system has population inversion.[7] In the latter case, one has laser gain instead of absorption at the pump frequency. We have implemented this concept in THz QCL sources based on intracavity DFG. Our first devices, which were reported in Ref. 7, produced only nanowatt-level THz output at $\lambda \approx 60\ \mu$m and operated up to 150 K. In this letter, we report THz DFG QCL sources with THz output power at $\lambda \approx 60\ \mu$m of approximately 7 μW at 80 K and still approximately 300 nW at RT.

Our devices are based on an $In_{0.53}Ga_{0.47}As/In_{0.52}Al_{0.48}As$ heterostructure grown by molecular beam epitaxy (MBE), with upper InP waveguide cladding regrown by metalorganic chemical vapor deposition (MOCVD). The MBE growth started on an InP substrate, n-doped to 9×10^{16} cm^{-3}, with 30 stages of the "double-phonon resonance" active region,[11] designed to emit at 10.5 μm, followed by 100-nm-thick GaInAs spacer, n-doped to 3×10^{16} cm^{-3}, and 30 stages of the "bound-to-continuum" active region,[11] designed to emit at 8.9 μm. The layer sequences for the two sections are listed in the captions of Fig. 1. The MBE growth ended with a 50-nm-thick GaInAs layer, n-doped to 3×10^{16} cm^{-3}. An upper waveguide cladding, consisting of 3.5-μm-thick and 0.2-μm-thick InP layers, n-doped to 5×10^{16} and 5×10^{18} cm^{-3}, respectively, was then overgrown by MOCVD.

The bound-to-continuum section in our devices is expected to have the largest $\chi^{(2)}$ for DFG. The conduction-band diagram of a single period of this section, along with the schematics of the THz DFG process, is shown in Fig. 1. For a resonant DFG, the expression for the nonlinear susceptibility[5,7] simplifies to

a)Electronic mail: mbelkin@seas.harvard.edu.
b)Electronic mail: capasso@seas.harvard.edu.

 © 2008 American Institute of Physics

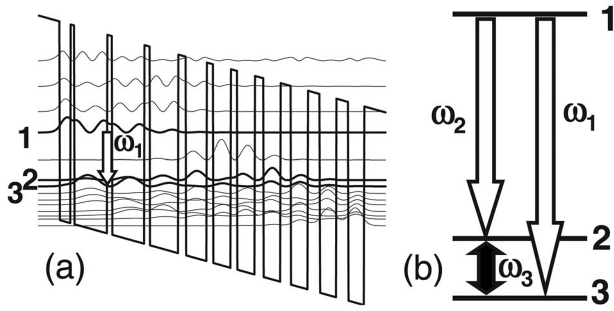

FIG. 1. (a) Calculated conduction-band diagram of one period of a bound-to-continuum quantum cascade laser section at applied bias of 37 kV/cm. The wavy curves represent the moduli squared of the wavefunctions. The electron states important for DFG are shown in bold and labeled 1 to 3. The layer sequence (in nm), starting from the injection barrier, for this structure is **4.0**/2.4/**0.7**/6.5/**0.8**/6.4/**0.8**/5.8/**2.2**/4.0/**1.3**/3.8/**1.4**/3.7/**1.5**/3.6/**1.9**/3.6/**2.5**/3.6/**2.5**/3.5. (The layer sequence for one period of a double-phonon resonance section which generates frequency ω_2 is **4.0**/2.0/**0.7**/6.0/**0.9**/5.9/**1.0**/5.2/**1.4**/3.8/**1.2**/3.2/**1.2**/3.2/**1.6**/3.1/**1.9**/3.1/**2.2**/3.0/**2.2**/2.9.) The barriers are indicated in bold face and the underlined layers are doped to $n=3\times10^{17}$ cm^{-3}. (b) Diagram showing the DFG process between the electron states in the bound-to-continuum section.

$$\chi^{(2)}(\omega_3=\omega_1-\omega_2)\approx\frac{e^3}{\hbar^2\varepsilon_0}\frac{z_{12}z_{23}z_{31}}{(\omega_3-\omega_{23}+i\Gamma_{23})}\times\left[\frac{N_1-N_3}{(\omega_1-\omega_{13}+i\Gamma_{31})}+\frac{N_1-N_2}{(-\omega_2+\omega_{12}+i\Gamma_{21})}\right], \tag{2}$$

where N_i are the population densities in the electron states $i=1$, 2, and 3, see Fig. 1, ez_{ij}, ω_{ij}, and Γ_{ij} are the dipole matrix element, frequency, and broadening of the transition between states i and j. Assuming $N_2\approx N_3$ for simplicity, both population differences in Eq. (2) are equal to the population inversion density ΔN which can be determined from a "gain=loss" condition. The laser gain in a medium with population inversion is given by the expression[5]

$$g(\omega_1)=\frac{\omega_1}{cn_{\text{eff}}(\omega_1)}\frac{\Delta Ne^2}{\varepsilon_0\hbar}\sum_n\frac{|z_{1n}|^2}{(\omega_1-\omega_{1n})+i\Gamma_{1n}}, \tag{3}$$

where $n_{\text{eff}}(\omega_1)$ is the effective refractive index of the laser mode and n refers to lower laser levels. A gain=loss condition for a QCL reads[12]

$$g_{\max}\Gamma=\alpha_{\text{wg}}+\alpha_m, \tag{4}$$

where $g_{\max}$ is peak of the laser gain in Eq. (3), Γ is the modal overlap factor with an active region, α_{wg} and α_m are waveguide and mirror losses, respectively. We estimate for our devices $\Gamma\approx0.4$, $\alpha_{\text{wg}}\approx8$ cm^{-1}, and $\alpha_m\approx3$ cm^{-1} and obtain $g_{\max}\approx28$ cm^{-1}. Assuming $\Gamma_{ij}\approx7.5$ meV, from Eqs. (2)–(4), we obtain that $\Delta N\approx2\times10^{15}$ cm^{-3} and $|\chi^{(2)}|\approx4\times10^4$ pm/V for the DFG in our devices. This value is two times larger than that calculated using the same formalism[13] for devices and a DFG process reported in Ref. 7.

The waveguide design in our devices has also been improved in comparison with that in Ref. 7. First, we have reduced doping in the QCL structure, which results in smaller THz losses. Second, the waveguide is now designed for phase matching, $k_3=k_1-k_2$, through controlling the waveguide cladding layers doping and thickness as well as the doping of the substrate. Using the effective refractive indices calculated for the TM_{00} modes of mid-IR pumps and a THz wave, as well as the THz mode losses, we estimate l_{coh} [see Eq. (1)] in our devices to be approximately 50–80 μm in 25–60-μm-wide ridges, which is approximately three times larger than that in Ref. 7. The limiting factor for l_{coh} in our case is the THz waveguide losses, which are calculated to be $\alpha\approx250$ cm^{-1}. We note that α can be reduced to below 100 cm^{-1} through further reduction of the doping in the substrate, waveguide layers, and active region.

Our material was processed into deep etched ridge waveguides 2 mm long and 25 μm wide, tapered to 60 μm toward the front facet, with a 400-nm-thick Si_3N_4 insulating layer on the lateral walls of the ridge and a Ti/Au (20 nm/400 nm) top contact [Figs. 2(a) and 2(b)]. A Ge/Au contact was deposited on the back. An Al_2O_3/Au (200 nm/50 nm) high-reflectivity coating was evaporated at the back facet of the devices. Tapering was introduced in order to improve the outcoupling efficiency of THz radiation from the waveguide.[14] The calculated waveguide modes for mid-IR and THz waves, along with the waveguide refractive index profile, are shown in Fig. 2(c).

For measurements, devices were operated in a pulsed mode with 60 ns pulses at a 250 kHz repetition rate. Radiation was collected using two 2 in. diameter parabolic mirrors: one with a 5 cm focal length to collect light from the device and the other with a 15 cm focal length to refocus it onto a thermopile or mercury-cadmium-telluride (MCT) detector for mid-IR measurements or a He-cooled calibrated silicon bolometer for THz measurements. Mid-IR powers were corrected for the 70% collection efficiency of our setup. Spectra were taken with a Fourier transform infrared spectrometer. For THz measurements, mid-IR radiation was blocked using optical filters. Our devices operated at dual wavelength up to RT. The current-voltage characteristic, the dependence of the product of the two mid-IR pump powers, $W(\omega_1)\times W(\omega_2)$, on current, and a typical emission spectrum for a typical device are shown in Fig. 3(a). The THz emission

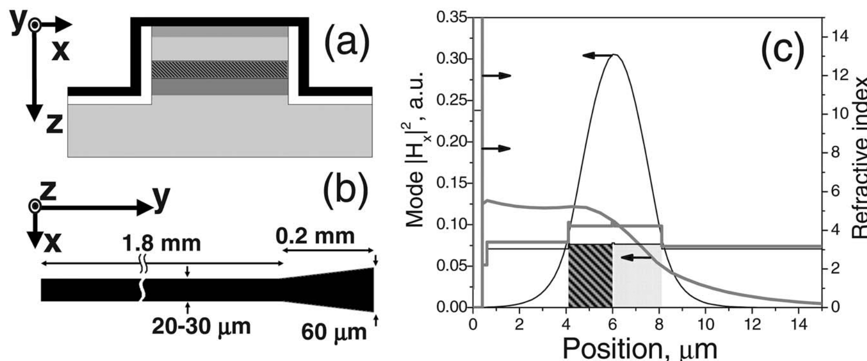

FIG. 2. (a) Waveguide structure: the gold layer is shown in black, the insulating Si_3N_4 layer is in white, and the semiconductor is in gray (for low-doped InP layers) and dark grey (for a high-doped InP layer and the two active region sections). The bound-to-continuum section is shaded. (b) Ridge waveguide shape, viewed from top: the back facet (left side) has a high-reflection coating. (c) The magnetic field intensity in the TM00 waveguide mode (left axis) and the refractive index profile (right axis) for $\lambda=8.9$ μm (thin black line) and $\lambda=60$ μm (thick gray line). Also shown in gray are the two sections of the active region.

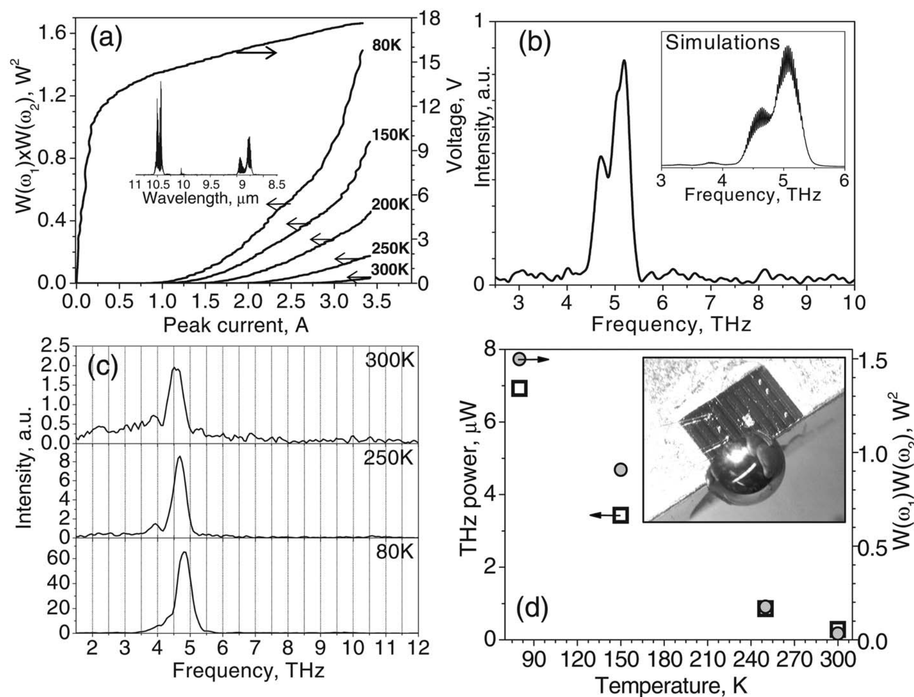

FIG. 3. (a) Product of mid-IR pump intensities vs current (left axis) and current-voltage (right axis) characteristics of a representative device. Inset: mid-IR emission spectrum of the device at 80 K. (b) Terahertz emission spectrum of the device in (a), measured at 80 K. Inset: THz DFG spectrum simulated from mid-IR spectrum in (a). (c) Terahertz emission spectra of a device with a Si hyperhemispherical lens attached to the facet at different temperatures. (d) Temperature dependence of the measured THz DFG signal power (left axis) and the product of mid-IR pump powers for a device with a Si lens. Inset: photograph of a device with a Si lens attached to a facet. The measurements in (d) and all the spectral measurements were done with a device operated with 3.5 A current pulses.

spectrum at 80 K of the same device is shown in Fig. 3(b). For comparison, we also show in Fig. 3(b) a THz DFG spectrum, simulated using the mid-IR spectrum in Fig. 3(a).

Because of subwavelength THz mode confinement in the waveguide [see Fig. 2(c)], the THz DFG output from our devices is expected to be strongly divergent and THz outcoupling efficiency may be poor.[14] Recently, Lee *et al.*[15] demonstrated that a silicon hyperhemispherical lens, attached to the device facet, may help to resolve these problems. We have equipped selected devices with a 2 mm diameter, 1.19 mm height high-resistivity silicon hyperhemispherical lens. The lens was positioned to within 5 μm of a device facet, following a procedure similar to that in Ref. 15. For lens alignment, we imaged the mid-IR output from our devices with a MCT detector. Devices with a lens demonstrated a 25-fold increase in collected THz DFG power output, compared to devices without a lens. The increase stems from improved collection efficiency [from below 10% to approximately 50%, see Ref. 15] and improvements in THz outcoupling efficiency. Typical THz DFG spectra of a device with a lens, collected at different temperatures, are shown in Fig. 3(c). The spectra are slightly different from that shown in Fig. 3(b) because mid-IR emission spectra vary from device to device. Terahertz output was observed up to RT, with THz power, corrected for the estimated 50% collection efficiency, decreasing from approximately 7 μW at 80 K to approximately 300 nW at RT. This trend is demonstrated in Fig. 3(d), where we also plotted a product of mid-IR pump powers at different temperatures. The data in Fig. 3(d) indicate that the drop in THz power output originates mostly from a decrease in mid-IR pump powers [see Eq. (1)], while THz DFG conversion efficiency remains constant, $\sim 5\ \mu\mathrm{W/W}^2$. Since mid-IR QCLs with cw power output levels of 1.5 W at RT have already been demonstrated, it appears that a THz QCL source with microwatt-level cw THz output at RT is within reach. We believe that further device optimization, including the utilization of the surface-emission scheme[16] for the THz radiation extraction, may lead to THz DFG QCLs providing up to a milliwatt of the THz output power at RT.

The structures were processed in the Center for Nanoscale Science in Harvard University, which is a member of the National Nanotechnology Infrastructure Network. This work was supported by AFOSR under Contract No. FA9550-05-1–0435. Sample growth was partly done in the University of Neuchatel. The authors would like to acknowledge help of Nicolas Hoyler.

[1]E. Bründermann, D. R. Chamberlin, and E. E. Haller, Appl. Phys. Lett. **76**, 2991 (2000).
[2]R. Köhler, A. Tredicucci, F. Beltram, H. E. Beere, E. H. Linfield, A. G. Davies, D. A. Ritchie, R. C. Iotti, and F. Rossi, Nature (London) **417**, 156 (2002).
[3]B. S. Williams, Nat. Photonics **1**, 517 (2007).
[4]M. A. Belkin, J. A. Fan, S. Hormoz, F. Capasso, S. P. Khanna, M. Lachab, A. G. Davies, and E. H. Linfield, Opt. Express **16**, 3242 (2008).
[5]Y. R. Shen, *The Principles of Nonlinear Optics* (Wiley, New York, 1984).
[6]See, e.g., K. L. Vodopyanov, M. M. Fejer, X. Yu, J. S. Harris, Y.-S. Lee, W. C. Hurlbut, and V. G. Kozlov, Appl. Phys. Lett. **89**, 141119 (2006).
[7]M. A. Belkin, F. Capasso, A. Belyanin, D. L. Sivco, A. Y. Cho, D. C. Oakley, C. J. Vineis, and G. W. Turner, Nat. Photonics **1**, 288 (2007).
[8]A. Lyakh, C. Pflügl, L. Diehl, Q. J. Wang, F. Capasso, X. J. Wang, J. Y. Fan, T. Tanbun-Ek, R. Maulini, A. Tsekoun, R. Go, and C. K. N. Patel, Appl. Phys. Lett. **92**, 111110 (2008).
[9]C. Gmachl, A. Belyanin, D. L. Sivco, M. L. Peabody, N. Owschimikow, A. M. Sergent, F. Capasso, and A. Y. Cho, IEEE J. Quantum Electron. **39**, 1345 (2003).
[10]C. Sirtori, F. Capasso, J. Faist, L. N. Pfeiffer, and K. W. West, Appl. Phys. Lett. **65**, 445 (1994).
[11]J. Faist, D. Hofstetter, M. Beck, T. Aellen, M. Rochat, and S. Blaser, IEEE J. Quantum Electron. **38**, 533 (2002).
[12]C. Gmachl, F. Capasso, D. L. Sivco, and A. Y. Cho, Rep. Prog. Phys. **64**, 1533 (2001).
[13]In Ref. 7, we assumed that all the electrons introduced by the intentional doping in the quantum cascade structure are in the upper laser state. This approach overestimates the actual second-order nonlinear susceptibility in the structure. The approach used in this work provides a better estimate.
[14]S. Kohen, B. S. Williams, and Q. Hu, J. Appl. Phys. **97**, 053106 (2005).
[15]A. W. M. Lee, Q. Qin, S. Kumar, B. S. Williams, Q. Hu, and J. L. Reno, Opt. Lett. **32**, 2840 (2007).
[16]J. A. Fan, M. A. Belkin, F. Capasso, S. Khanna, M. Lachab, A. G. Davies, and E. H. Linfield, Opt. Express **14**, 11672 (2006).